Energy
Advances

PAPER

View Article Online
View Journal | View Issue

Cite this: *Energy Adv.*, 2023, 2, 679

Graphene oxide based nickel–copper–zinc and copper–zinc cobaltite: catalysts for the thermolysis of ammonium perchlorate and nitrotriazolone†

Pragnesh N. Dave * and Ruksana Sirach

Received 25th January 2023,
Accepted 27th March 2023

DOI: 10.1039/d3ya00045a

rsc.li/energy-advances

The mixed transition metal cobaltites copper–zinc cobaltite ($CuZnCo_2O_4$) and nickel–copper–zinc cobaltite ($NiCuZnCo_2O_4$) were synthesized using the co-precipitation method. The diffraction, electronic, polarization, and vibrational properties of the prepared $NiCuZnCo_2O_4$ and $CuZnCo_2O_4$ were recorded using X-ray diffraction (XRD), UV-visible spectrophotometry (UV-Vis), Raman scattering, and infrared spectrophotometry, respectively. Graphene oxide (GO) based cobaltites were prepared by mechanical grinding using $NiCuZnCo_2O_4$ and $CuZnCo_2O_4$ to produce $NiCuZnCo_2O_4$ + GO and $CuZnCo_2O_4$ + GO, respectively. Catalytic activities of four compositions for the thermal decomposition of ammonium perchlorate (AP) and nitrotriazolone (NTO) were analyzed using thermal techniques such as differential scanning calorimetry (DSC), differential thermal analysis (DTA), and thermogravimetry (TG). The effect of spinels $NiCuZnCo_2O_4$ and $CuZnCo_2O_4$ and their mixtures with GO showed that their addition decreases exothermic peak temperatures of AP and NTO by ~50 °C to 150 °C compared to that with pure AP and NTO. The simple synthesis method of these catalysts helps laboratory-scale to industrial-scale production for the preparation of different chemical propulsion systems.

1. Introduction

Ammonium perchlorate (AP) is one of the most widely employed energetic materials in hydroxyl-terminated polybutadiene-based solid rocket propellants owing to AP's high energetic performance.[1–4] The continuously increasing demands for fast combustion of propellant oxidizers, the inadequate availability, and high sensitivity of other high energetic materials such as 1,3,5,7-tetranitro-1,3,5,7-tetrazocane (HMX) and 1,3,5-trinitro-1,3,5-triazine (RDX) have been directed to the modifications of high energetic materials such as AP and nitrotriazolone (NTO) to formulate efficient chemical propulsion oxidizers and/or insensitive explosives that are easily available, provide excellent performance, and possess good compatibility with the energetic system. NTO is often employed in insensitive munition (IM) formulations such as IMX 101 and IMX 104 along with other high energetic materials such as 2,4-dinitroanisole, nitroguanidine, and RDX to name a few because of its low sensitivity.[5] NTO is an insensitive energetic material that is synthesized in a laboratory using a safe and low-cost process. On the other hand, AP is a strong oxidizer that has ease of availability.[6–10] However, there are certain limitations such as AP has a wide temperature range leading to a slower decomposition process and NTO has a high activation energy barrier.[6,11,12] Previous reports have mentioned that the thermal performance of highly energetic materials can be improved using energetic co-crystals, addition of catalysts, and reducing the size of highly energetic formulations.[6,7,11–15] Moreover, the improvement in the thermal decomposition of highly energetic materials can directly influence the combustion performance of the corresponding energetic formulations.[16–18] The use of these approaches or their combinations can influence the thermal and kinetic parameters of the decomposition of highly energetic materials such as AP and NTO. The addition of simple catalysts such as metal oxides or their composites with carbon-based materials such as multi-walled carbon nanotubes (MWCNTs) and graphene oxides (GO) is one of the efficient ways to improve the thermo-kinetic parameters of the decomposition of AP and NTO compared to forming a new co-crystal or reducing the size due to safety risks.[6,11,12] It was observed that the carbon-based materials themselves do not have a much greater impact on the thermal decomposition of NTO or AP, but they can provide better results in the presence of metal oxides having active metal centers because of the synergetic effect.[11,12] Moreover, the nanosized metal oxide catalyst containing

---

Department of Chemistry, Sardar Patel University, Vallabh Vidyanagar, 388 120, Gujarat, India. E-mail: pragnesh7@yahoo.com

† Electronic supplementary information (ESI) available. See DOI: **https://doi.org/10.1039/d3ya00045a**

energetic formulations can provide better thermal performance than the micron-size catalyst. For example, Chalghoum *et al.*,[16] have reported that the use of nanosized copper oxide (CuO) can be a better catalyst for improving the thermal performance of composite solid propellants compared to micron-size CuO.

Mono, binary, and ternary transition metal ferrites and cobaltite nanomaterials are widely used on a large scale today for novel and efficient applications in nanoscience, nanotechnology, catalysis, and many more.[19–22] Recently, in these nanomaterials, spinel structure nanoparticles with binary and ternary transition metal cobaltite (MCo_2O_4; M = metal ions) materials have been developed as efficient promising redox catalysts. Due to their nanosize, ability to serve as an effective electron carrier, and ability to stabilize oxidizers during decomposition, these catalysts can improve the thermal decomposition process of AP and NTO.[13,23–25]

Catalytic materials with strong catalytic efficiency such as metals, alloys, metal oxides, and spinel ferrites have been used for a long time. As a potential alternative for these materials, mixed transition metal-based spinel systems have attracted great attention because they have good optical properties in terms of easy-to-accept electrons and fast movement of electrons in the various empty electron orbitals.[26–28] Additionally, the presence of mixed transition metals' synergistic effect helps to improve the catalytic performance more than that of the single metal spinel. Spinel cobaltite has recently drawn considerable attention because of its tremendous physicochemical properties and huge applications in the field of catalysis, electronic devices, sensors, and many more. There are mainly four types of cobalt oxides, namely cobalt oxide (CoO), di-cobalt trioxide (Co_2O_3), tricobalt tetroxide (Co_3O_4), and di-cobalt tetroxide (Co_2O_4). Spinel cobalt oxide or cobaltite (Co_3O_4 or MCo_2O_4) has been widely important as a catalyst and an electrode material used in future applications of supercapacitors, thermolysis of propellants, batteries, *etc.*, due to its promising high conductivity and multiple oxidation states, which lead to high redox activity.[29–32] This characteristic makes cobaltite an efficient and excellent material. Cobaltite can be synthesized using various methods such as hydrothermal, solvothermal, sol–gel, and co-precipitation. Transition metal-mixed cobaltite materials with nanostructured, synergistic effects and enhanced catalytic reactivity are particularly attractive for application in the thermal decomposition of AP and NTO.[33–35]

In this research work, binary and ternary transition metal cobaltite such as $CuZnCo_2O_4$ and $NiCuZnCo_2O_4$ were prepared *via* a simple, low-cost, less time-consuming co-precipitation method. The physicochemical characteristics of these cobaltites were investigated using various characterization tools. We synthesized spinel cobaltite to investigate their catalytic performance on the thermal decomposition of AP and NTO in detail as future applications in the formulation of various chemical propulsion systems. Further, the preliminary analysis of the catalytic mechanism, kinetics, and thermodynamics is discussed.

2. Experimental sections

2.1. Preparation of cobaltite $CuZnCo_2O_4$ and $NiCuZnCo_2O_4$

Cobalt (II) nitrate hexahydrate ($Co(NO_3)_2{\cdot}6H_2O$), nickel (II) nitrate hexahydrate ($Ni(NO_3)_2{\cdot}6H_2O$), cupric (II) nitrate trihydrate ($Cu(NO_3)_2{\cdot}3H_2O$), and zinc (II) nitrate hexahydrate ($Zn(NO_3)_2{\cdot}6H_2O$) of ∼98–99% purity were acquired from SRL Pvt. Ltd. and were used as received. Initially, 0.02 M $Co(NO_3)_2{\cdot}6H_2O$ and 0.01 M quantity of metal nitrate salts $Cu(NO_3)_2{\cdot}3H_2O$, and $Zn(NO_3)_2{\cdot}6H_2O$ were homogeneously dissolved in the 50 mL of triple distilled water followed by dropwise addition of 0.2 M NaOH solution with continuous stirring at 70 °C temperature until complete precipitation of metal hydroxides occurred at pH ∼ 12–14. The $CuZnCo_2O_4$ precipitate was filtered, washed with triple distilled water, dried overnight, and calcined at 360 °C for 4 h at a heating rate of 2 °C min^{-1}. Similarly, $NiCuZnCo_2O_4$ was obtained by mixing 0.02 M $Co(NO_3)_2{\cdot}6H_2O$ with 0.01 M solutions of $Cu(NO_3)_2{\cdot}3H_2O$, ($Ni(NO_3)_2{\cdot}6H_2O$), and $Zn(NO_3)_2{\cdot}6H_2O$. The hydroxides of the metal ions were produced by adding 0.2 M NaOH until complete precipitation (∼12–14 pH) was obtained followed by washing, drying, and calcination (360 °C; 4 hours; 2 °C min^{-1} heating rate) of the precipitate. $NiCuZnCo_2O_4$ and $CuZnCo_2O_4$ were further mechanically mixed with graphene oxide (GO) in a 2 : 1 mass ratio using a mortar and pestle, to prepare GO-based cobaltite named $NiCuZnCo_2O_4$ + GO and $CuZnCo_2O_4$ + GO. Briefly, 1 g $NiCuZnCo_2O_4$ and $CuZnCo_2O_4$ were mixed with 0.5 g GO to produce $NiCuZnCo_2O_4$ + GO and $CuZnCo_2O_4$ + GO, respectively.

The four prepared catalysts ($NiCuZnCo_2O_4$, $CuZnCo_2O_4$, $NiCuZnCo_2O_4$ + GO, and $CuZnCo_2O_4$ + GO) were characterized to investigate their physicochemical properties. Mixing 0.002 g catalysts ($NiCuZnCo_2O_4$, $CuZnCo_2O_4$, $NiCuZnCo_2O_4$ + GO, and $CuZnCo_2O_4$ + GO) with 0.098 g AP or NTO using a mortar pestle formed eight energetic mixtures, namely $NiCuZnCo_2O_4$ + AP, $CuZnCo_2O_4$ + AP, $NiCuZnCo_2O_4$ + GO + AP, $CuZnCo_2O_4$ + GO + AP, $NiCuZnCo_2O_4$ + NTO, $CuZnCo_2O_4$ + NTO, $NiCuZnCo_2O_4$ + GO + NTO and $CuZnCo_2O_4$ + GO + NTO (Fig. 1). The catalytic influence of these catalysts on the thermal decomposition parameters of AP and NTO was investigated using simultaneous thermal analysis (TG-DTA-DSC).

2.2. Characterization techniques

The structural patterns of the four catalysts were categorized by powder X-ray diffraction (XRD) technique using a Rigaku Ultima IV model instrument with monochromatic Cu Kα radiation wavelength (λ) 1.5406 Å, at 40 mA and 40 kV between the diffraction angle in the range of 20° to 70°, and step size with 0.03°. The recorded patterns were analyzed by X'pert Highscore plus software and average crystallite sizes were calculated using the Debye–Scherrer equation (eqn (1)).[36]

$$D = \frac{0.9\lambda}{\beta\cos\theta} \quad (1)$$

Where D is termed as the crystal size, λ is termed as the wavelength of X-ray, θ is termed as the Braggs angle in radians,

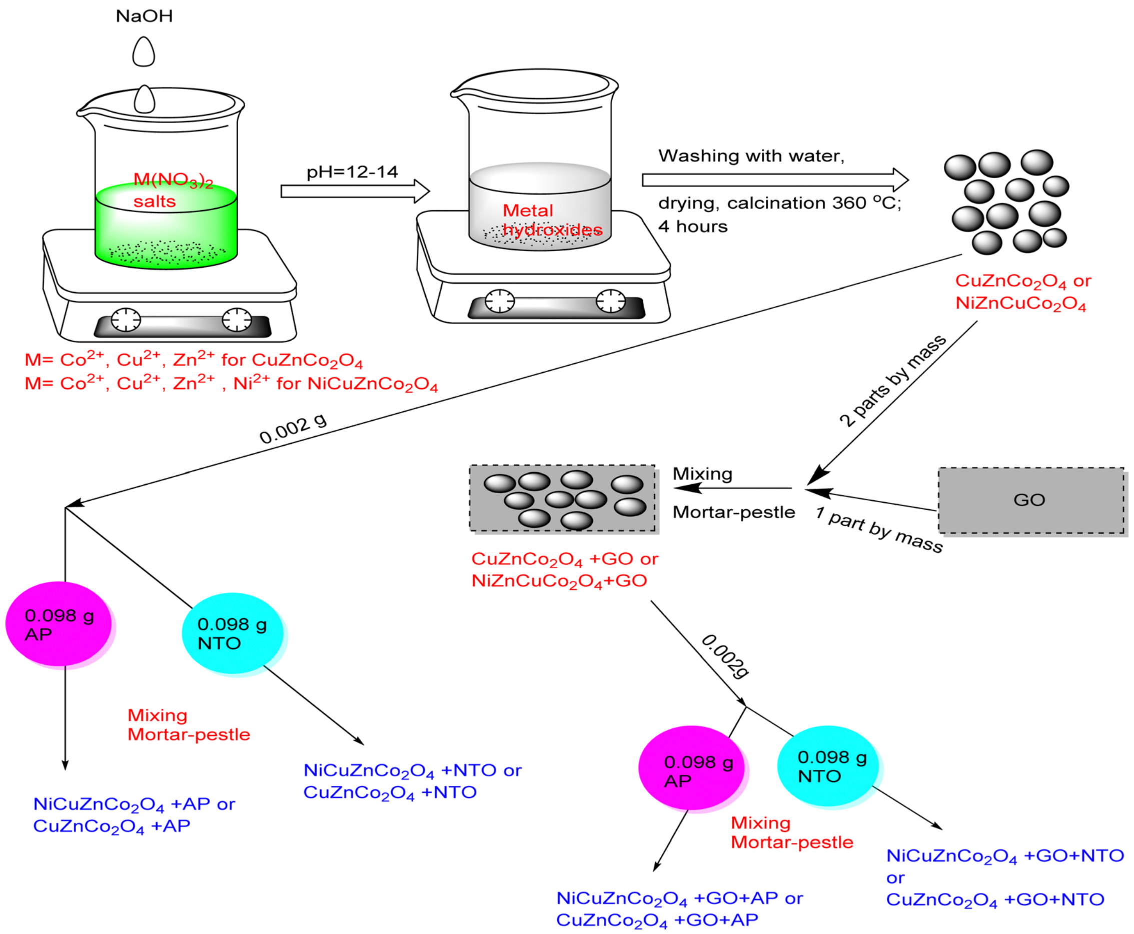

Fig. 1 Schematic presentation of the preparation of the catalysts and their mixture with AP and NTO.

and β is termed as the full width at half maximum (FWHM) of the peak in radians.

Optical absorption studies were conducted using an ultraviolet-visible (UV-Vis) spectrophotometer model 160-A of Shimadzu Pte Ltd., Japan. Raman spectra of all nanocatalysts were obtained using a LabRam Dilor spectrometer using a 530 nm laser source. The molecular vibrational characteristics of nanomaterials were studied using the ABB MB 3000 FT-IR laboratory spectrometer and spectra were recorded between 4000 cm^{-1} and 400 cm^{-1} wavenumbers using KBr pellets. For the pellet preparation, KBr, $NiCuZnCo_2O_4$, and $CuZnCo_2O_4$ samples were dried in an oven. The dried catalyst sample (either $NiCuZnCo_2O_4$ or $CuZnCo_2O_4$) was mixed with dried KBr in a 100 : 1 mass ratio using a mortar pestle until a homogenous mixture was formed followed by the formation of a pellet using a hydraulic press.

The catalytic proficiency of nano-cobaltite such as $NiCuZnCo_2O_4$ and $CuZnCo_2O_4$ for the thermal decomposition of AP and NTO was investigated by thermogravimetric analyzer-differential scanning calorimetry (TGA-DSC) on a 5000/2920 TA instrument, USA, at heating rates (β) = 5, 10, and 15 °C min^{-1} for NTO containing samples and at heating rates of 10, 15, and 20 °C min^{-1} for AP containing samples (the DSC curves of AP and NTO were measured at β = 10 °C min^{-1}) under N_2 atmosphere at a flow rate of 50 mL min^{-1} (sample mass = ∼4–5 mg).

The surface morphology of the four catalysts ($NiCuZnCo_2O_4$, $CuZnCo_2O_4$, $NiCuZnCo_2O_4$ + GO, and $CuZnCo_2O_4$ + GO) was studied using a field-emission scanning electron microscope (FEG-SEM; Nova NanoSEM 450; Make: FEI Ltd; 20 kV accelerating voltage).

3. Results and discussion

3.1. Structural studies

The powder XRD diffractograms of all four spinel cobaltite nanomaterials were used for identifying the phase and crystallinity behavior of the samples. Fig. 2, shows that the XRD pattern of catalysts $NiCuZnCo_2O_4$, $CuZnCo_2O_4$, $NiCuZnCo_2O_4$ + GO, and $CuZnCo_2O_4$ + GO cobaltite indicated that they are polycrystalline.

The calculated average crystallite sizes (D) from Debye Scherrer's equation (eqn (1))[36] for all samples were found in the range of ∼ 9 nm to 28 nm. In the presence of GO, an increment in the pattern broadness was observed, which corresponded to the decreased crystallinity of the resulting mixture ($NiCuZnCo_2O_4$ + GO and $CuZnCo_2O_4$ + GO) compared to those

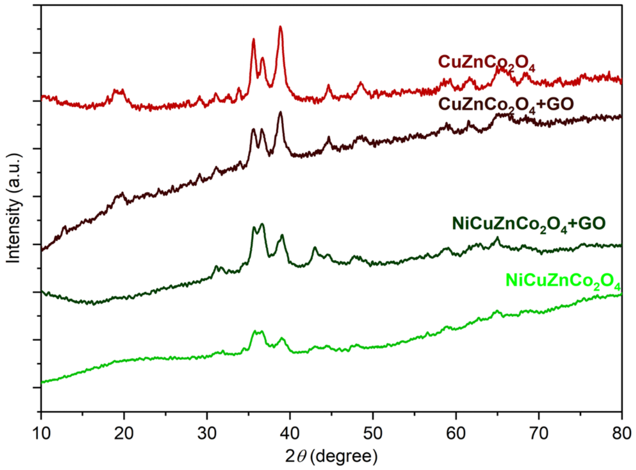

Fig. 2 Powder XRD patterns of binary ($CuZnCo_2O_4$) or ternary ($NiCuZnCo_2O_4$) transition metal cobaltite and their mixture with GO.

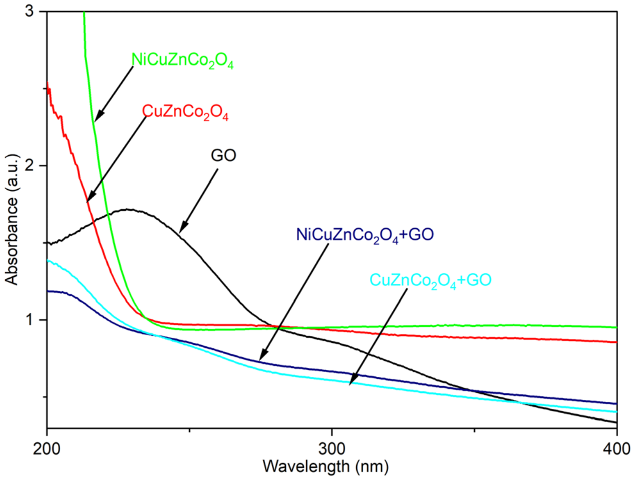

Fig. 3 UV-visible spectra of GO, cobaltites, and GO-based cobaltites.

of pure cobaltite ($NiCuZnCo_2O_4$ and $CuZnCo_2O_4$). The characteristic peaks of cobaltite were found between 30° to 40° 2 theta angles with few less intense peaks observed throughput 2θ = 10–70°. The six miller indices of the hkl planes of binary-ternary spinel cobaltites include (111), (220), (311), (222), (400), (422), (511), and (440) corresponding to 2 theta angles of ∼18°, ∼31°, ∼36°, ∼38°, ∼44°, ∼56°, ∼58°, and ∼64°, respectively. The (311) and (222) planes are extra random orientation intensive planes belonging to cubic, tetrahedral, and octahedral crystal phases of the transition metal-mixed spinel cobaltite material.[37,38] The intensities of the peaks found between 30° to 40°, 2theta angles were more intense due to the presence of more electron density. Moreover, with the increasing presence of the metal in the spinel cobaltite, the intensity of the peak decreased as shown in the XRD pattern of $NiCuZnCo_2O_4$ and $CuZnCo_2O_4$. The absence of additional impurity peaks in the XRD diffractogram confirmed the formation of the spinel cobaltite.

3.2. Optical studies

Binary and ternary spinel cobaltite nanomaterials structurally have tetrahedral and octahedral sites, which are made up of divalent and trivalent cations, respectively, associated with the creation of anti-site defects that is the main source of the electronic transition, which are energetically desirable.[39] The UV-visible spectra of the prepared spinel cobaltites with and without GO, such as $NiCuZnCo_2O_4$, $CuZnCo_2O_4$, $NiCuZnCo_2O_4$ + GO, $CuZnCo_2O_4$ + GO, and only GO were investigated in the wavelength range 200–400 nm using UV-visible spectrophotometry. Fig. 3, shows the variation in the absorbance of such cobaltites and GO-based cobaltites with the wavelength. The absorption spectra of GO, $NiCuZnCo_2O_4$, $CuZnCo_2O_4$, $NiCuZnCo_2O_4$ + GO, and $CuZnCo_2O_4$ + GO cobaltite nanomaterials display more absorption of light in the ultraviolet region.

These optical data were further used to estimate the optical band gap energy (E_g) value of the cobaltite nanomaterials from Tauc's relation (eqn (2)) as reported in this study.[40] The band gap energy increases between the valence band and the conduction band upon decreasing the crystalline size.

$$\alpha h\nu = A\left(h\nu - E_g\right)^{\frac{1}{2}} \quad (2)$$

where A is a constant and E_g is the optical band gap energy (eV). E_g is obtained by the variation of $(\alpha h\nu)^2$ *versus* $h\nu$ plot, which is a straight line in the domain of higher energies, indicating a direct optical transition. The observed direct band gap energy of cobaltite nanomaterials was found in the range of ∼5–6 eV, while the GO molecule exhibited an E_g value of around ∼4.0 eV. The high band gap energy values suggest that the energy gap between the valence band and the conduction band was high.

3.3. Raman scattering

Raman scattering generally gives information about vibrations within a molecule in terms of shifting of Raman shift, which is the difference in frequency between the laser light and the scattered light. Here, all nanomaterials are solids; thus their phonon modes can also be observed. The difference between photon energy in and out is not related to the wavelength of the laser source, which can be expressed as wavenumbers and structurally identified as the fingerprint region of Raman bands. Mainly, vibrational frequencies are specific to a molecule's chemical bonds and symmetry that identified the molecules in the wavenumber range of 500–1700 cm^{-1}.

In Raman spectra (Fig. 4), peaks shifting towards lower or higher wavenumber are assigned to the chemical bond length of molecules of $NiCuZnCo_2O_4$, $CuZnCo_2O_4$, $NiCuZnCo_2O_4$ + GO, and $CuZnCo_2O_4$ + GO nanomaterials.

The Raman shift at the lower wavenumber corresponds to a lower bond length or *vice versa*. Moreover, during analysis, if the presence of any internal or external effects is found, the change in the chemical bond length of molecules and shifting of the Raman shift may be observed. As shown in Fig. 4, the Raman spectra of cobaltite nanomaterials such as $NiCuZnCo_2O_4$ and $CuZnCo_2O_4$ showed broad peaks between 180–700 cm^{-1}

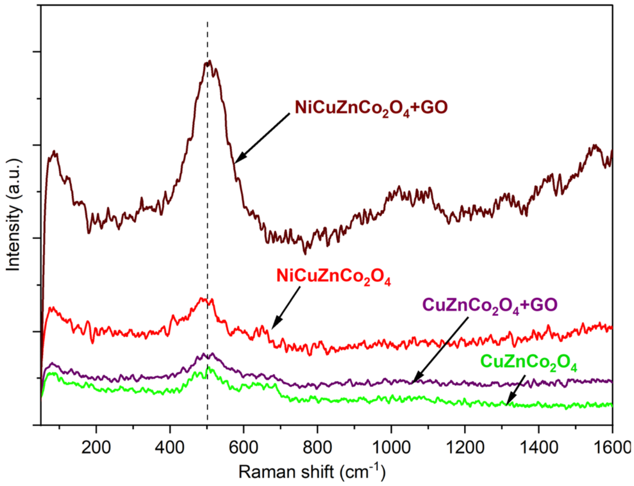

Fig. 4 Raman spectra of NiCuZnCo$_2$O$_4$ + GO, NiCuZnCo$_2$O$_4$, CuZnCo$_2$O$_4$ + GO, and CuZnCo$_2$O$_4$ cobaltite nanomaterials.

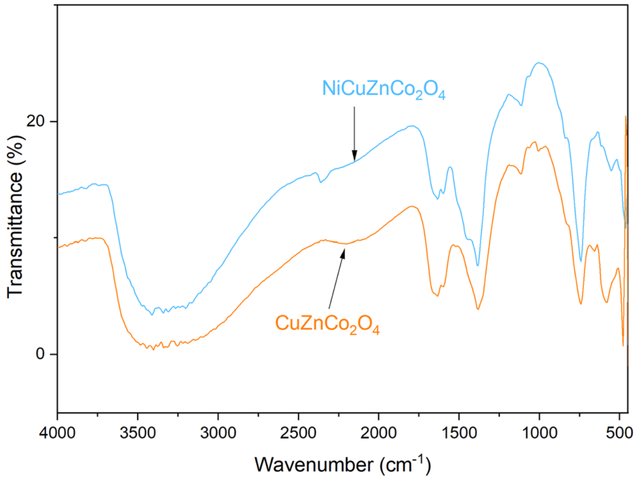

Fig. 5 . Fourier transform infrared (FT-IR) spectra of NiCuZnCo$_2$O$_4$ and CuZnCo$_2$O$_4$ cobaltite nanomaterials.

wavenumbers assigned to characteristic Raman-active modes of metal oxides. These are A_{1g}, E_g, and $3F_{2g}$ active modes, some modes are merged and gave a broad Raman peak.[41] However, cobaltites with GO nanomaterials such as NiCuZnCo$_2$O$_4$ + GO and CuZnCo$_2$O$_4$ + GO showed shifting of Raman peaks compared with cobaltites alone. Moreover, small peaks were also observed in the range of 1400–1650 cm^{-1} Raman shift due to the effect of GO molecules or these region peaks are characteristic peaks of GO molecules.[41] A slight shift in peak positions was observed for all Raman active modes concerning spinel cobaltites NiCuZnCo$_2$O$_4$ and CuZnCo$_2$O$_4$. In addition, the peak broadening and their shifting to the lower wavenumbers are associated with the high occupancy of transition metal ions in the octahedral sites or the internal effect of the GO molecule. In general, the presence of some unpolarized molecules such as water, metals, elements, and/or simple ionic compounds could not show any Raman signal.

3.4. Fourier transform-infrared (FT-IR) analysis

FT-IR spectra of NiCuZnCo$_2$O$_4$and CuZnCo$_2$O$_4$ obtained using the KBr pellet method are shown in Fig. 5. As shown in this spectrum, the molecular vibrational fingerprint of FT-IR bands were recorded in the spectral region of 4000–400 cm^{-1} wavenumbers. There are three regions of FT-IR bands: higher, moderate, and lower range wavenumbers. Bands observed at higher region (4000–2000 cm^{-1}) wavenumbers are associated with stretching vibrational modes, and moderate and lower region (<2000 cm^{-1}) wavenumbers are associated with bending vibrational modes. Both cobaltites have two peaks, which appeared between the 500–700 cm^{-1} region and were associated with the formation of metal–oxygen bonds in tetrahedral and octahedral sites in the spinel lattice. The peaks at ∼581 and 740 cm^{-1} were observed at slightly higher wavenumbers than those previously reported at 561 and 653 cm^{-1} for MnCo$_2$O$_4$ because of different metal constituents.[42] The peak at ∼740 cm^{-1} arises because of Co–O bond vibrations in the tetrahedral site and the peak at ∼581 cm^{-1} arises because of Cu–O, Zn–O, and/or Ni–O bond vibrations in the octahedral site. The appearance of these characteristic peaks confirmed the formation of cobaltite. The peaks become strong and broad, revealing the formation of spinel structure cobaltite.[42] The bands above 2000 cm^{-1} are due to the coordinated/entrapped water absorbed from the moisture during the storage process.[42] A strong band between 3600–3000 cm^{-1} arises because of OH stretching vibrations. Similarly, the peaks at 1000–1300 cm^{-1} and 1643 cm^{-1} are assigned to C–O/C=O stretching and bending vibrations attributed to adsorbed gaseous molecules within the cobaltite. This also authenticated the formation of the pure spinel structure, which is in good accordance with the XRD results. This result further demonstrated the preparation of binary-ternary transition metal cobaltite nanomaterials.

3.5. Morphological investigation

The SEM image of NiCuZnCo$_2$O$_4$ (Fig. 6a) revealed that NiCuZnCo$_2$O$_4$ had cubic morphology with most particles falling below 100 nm in size. The analysis of the SEM image suggested that most particles of NiCuZnCo$_2$O$_4$ fall between 57–80 nm in size. Particles were well distributed with a narrow size distribution. NiZnCo$_2$O$_4$ aggregated particles on the surface of GO were observed in the SEM image of NiZnCo$_2$O$_4$ + GO (Fig. 6b). The aggregation of NiCuZnCo$_2$O$_4$ makes it difficult to correctly identify the morphology of NiZnCo$_2$O$_4$ + GO. The SEM image of CuZnCo$_2$O$_4$ (Fig. 6c) shows a layered structure with wire-like morphology at the left corner of the SEM image. The width of the layers/wire falls in the 40–100 nm range. The SEM images of both NiCuZnCo$_2$O$_4$ and CuZnCo$_2$O$_4$ confirm their nano-size. The particle size was larger than the crystalline size (9–28 nm) of NiCuZnCo$_2$O$_4$ and CuZnCo$_2$O$_4$. Elongated particles of CuZnCo$_2$O$_4$ are visible in the SEM images of CuZnCo$_2$O$_4$ + GO (Fig. 6-d). The morphology of CuZnCo$_2$O$_4$ + GO was similar to that obtained for CuZnCo$_2$O$_4$.

3.6. Thermal analyses

The catalytic behavior of binary-ternary cobaltite nanomaterials such as NiCuZnCo$_2$O$_4$ and CuZnCo$_2$O$_4$ with and without GO on

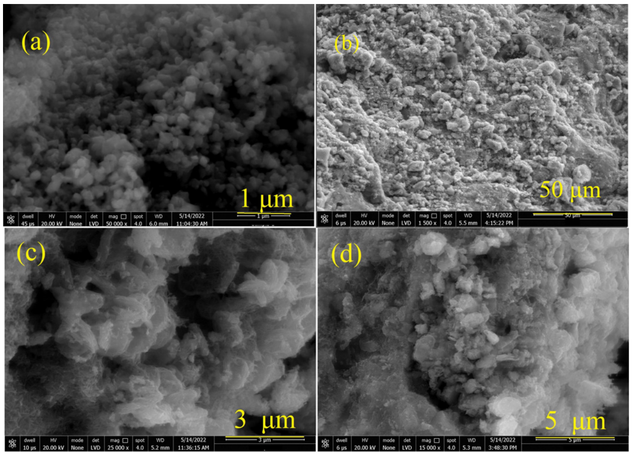

Fig. 6 SEM images of (a) $NiCuZnCo_2O_4$; (b) $NiCuZnCo_2O_4$ + GO (c) $CuZnCo_2O_4$; and (d) $CuZnCo_2O_4$ + GO.

the thermal decomposition of AP and NTO was investigated through TG-DTA-DSC experiments. Here, the DTA and DSC thermographic patterns of all the samples were similar but the difference was observed only in the decomposition peak temperature. The DSC curves of pure AP and NTO are shown in Fig. 7 while their decomposition in the presence of catalysts $NiCuZnCo_2O_4$, $NiCuZnCo_2O_4$ + GO, $CuZnCo_2O_4$, and $CuZnCo_2O_4$ + GO are shown in Fig. 8–11.

The DSC curve (Fig. 7) revealed that the thermal decomposition of pure AP occurred in two stages while that of pure NTO occurs in a single stage (Fig. 7-b). The first endothermic peak at ~247 °C in the DSC curve of AP (Fig. 7-a) belongs to the crystallographic transition of AP from orthorhombic to cubic.[43] Two exothermic curves belong to low-temperature thermal decomposition (LTD) and high-temperature thermal decomposition (HTD) of AP. Partial decomposition of AP and the formation of an intermediate product is assigned to the first exothermic peak (LTD) appearing at ~320 °C (Chemical eqn (3)). The second exotherm at ~439 °C temperature indicates that the main decomposition peak was assigned to the complete decomposition of the intermediate product into gaseous products.[43,44] The insensitive high energetic material nitrotriazolone (NTO) thermal decomposition revealed a single sharp exothermic peak at ~276 °C.[45] DSC curves of AP and NTO were in accordance with those from previous literature.[6,11] The LTD decomposition of AP is attributed to proton transfer from NH_4^{+1} to ClO_4^{-1} (chemical eqn (3)). During LTD, a small amount of NH_4ClO_4 can directly decompose to yield gaseous products such as N_2, Cl_2, and N_2O, leading to a small mass loss. In the HTD step, which is a major decomposition step, NH_3, and $HClO_4$ decompose to produce various gaseous products (NO_2, O_2, N_2O, H_2O, Cl_2, NO) and release high heat.[6,12]

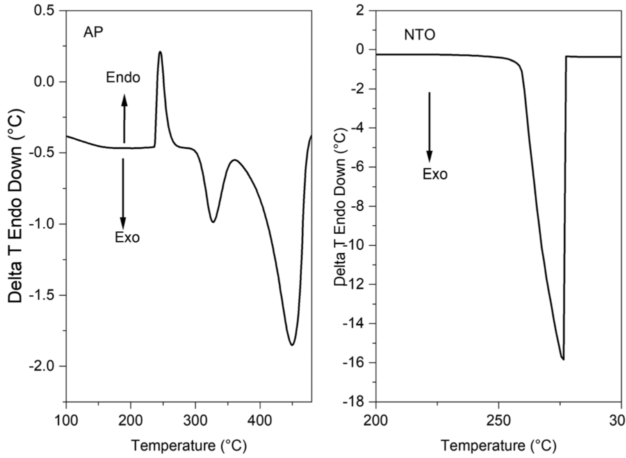

Fig. 7 Thermal decomposition of pure AP and NTO.

$$NH_4ClO_4 \rightarrow NH_3\text{–}H\text{–}ClO_4 \rightarrow NH_3\text{–}HClO_4 \rightarrow NH_3 + HClO_4 \rightarrow \text{gaseous products} \quad (3)$$

Fig. 8 and 9 show the catalytic effect of $NiCuZnCo_2O_4$ and $NiCuZnCo_2O_4$ + GO on the decomposition temperature of AP and NTO. Four catalysts were stable under the thermal decomposition range of AP and NTO compositions containing the catalysts (Fig. S1, ESI†). At a heating rate of 10 °C min^{-1}, the DSC exothermic decomposition peak temperatures of $NiCuZnCo_2O_4$ (Fig. 8a) and $NiCuZnCo_2O_4$ + GO + NTO (Fig. 9a) appeared around ~250 °C and ~265 °C, respectively, suggesting low-temperature decomposition of NTO. Moreover, in the DSC curves of $NiCuZnCo_2O_4$ + GO + NTO, an additional endothermic peak, and an exothermic peak were observed. The endothermic peak below 100 °C was observed because of a loss of moisture accompanied by 7% mass loss (TG thermograph). Additional exothermic peak observed in the DSC curve of $NiCuZnCo_2O_4$ + GO + NTO at ~227 °C can be assigned to the loss of volatile impurities or hydroxyl (–OH) from the surface of the catalyst. The decomposition of $NiCuZnCo_2O_4$ + AP and $NiCuZnCo_2O_4$ + GO + AP takes place in a single step as opposed to AP, in which two exothermic curves were obtained. This was because the catalysts impacted the HTD to very low temperatures resulting in a merger of two exothermic curves into a single DSC curve. An endothermic peak below <100 °C in the DSC curve of $NiCuZnCo_2O_4$ + AP was assigned to the loss of water (7% mass loss) molecules. The exothermic decomposition curve of $NiCuZnCo_2O_4$ + AP (Fig. 8b) was observed at ~300 °C. For the same heating rate, the DSC endothermic and exothermic decomposition peak of AP in the presence of catalyst $NiCuZnCo_2O_4$ + GO (Fig. 9b) appeared around ~276 °C. No change in the endothermic transition temperature of AP was observed in the presence of $NiCuZnCo_2O_4$ + GO and $NiCuZnCo_2O_4$, indicating no significant impact of these catalysts on the endothermic peak. A significant impact of these catalysts on the reduction of the exothermic decomposition peak temperature of AP was observed. Moreover, ternary transition metal spinel cobaltite ($NiCuZnCo_2O_4$) was the more efficient catalyst for the thermal decomposition of NTO while this cobaltite with GO ($NiCuZnCo_2O_4$ + GO) was more suitable for the thermolysis of AP. The reason behind this may be that ternary spinel cobaltite provides active and nano-sized particles for the redox mechanism during NTO's thermolysis, and in the

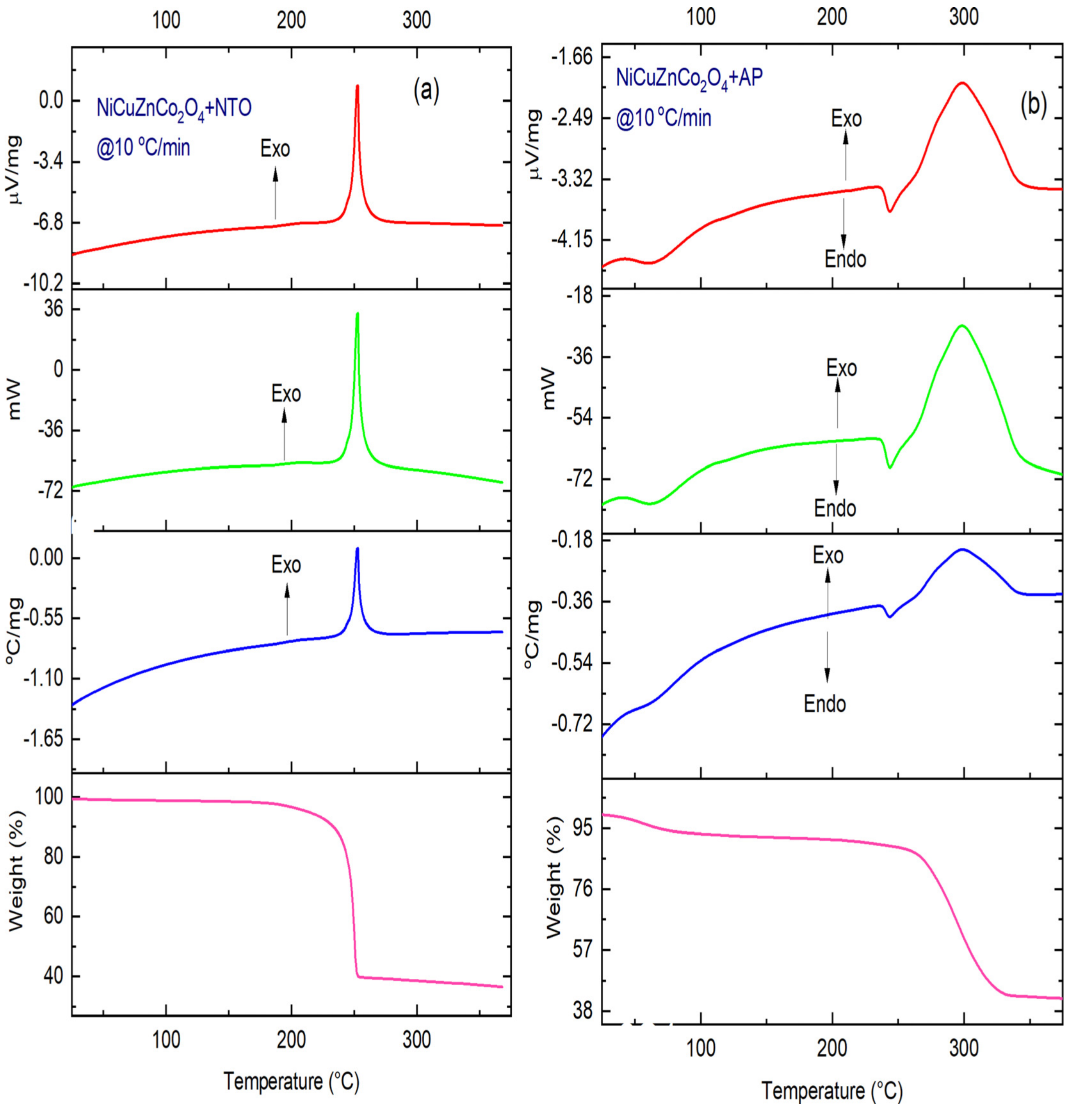

Fig. 8 TG-DTA-DSC thermographs of (a) $NiCuZnCo_2O_4$ + NTO and (b) $NiCuZnCo_2O_4$ + AP at 10 °C min^{-1} heating rate.

presence of GO, this cobaltite showed a fast electron transfer mechanism during AP's decomposition. In the presence of these catalysts, the single-phase exothermic decomposition of AP was observed. The mass losses in the exothermic decomposition of $NiCuZnCo_2O_4$ + NTO and $NiCuZnCo_2O_4$ + GO + AP were ~60% and ~90% for NTO and AP, respectively.

Fig. 10 and 11, show the catalytic effect of binary spinel cobaltite $CuZnCo_2O_4$ and $CuZnCo_2O_4$ + GO on the decomposition temperature of AP and NTO. $CuZnCo_2O_4$ + NTO (Fig. 10a) exhibits one endothermic curve <100 °C owing to the loss of moisture content (4% mass loss). The two exotherms at 225 °C and 257 °C correspond to the thermal decomposition of NTO. Similarly, for $CuZnCo_2O_4$ + GO + NTO (Fig. 11a), an endothermic peak below 100 °C corresponds to the loss of adsorbed moisture, and the main decomposition peak (~220 °C) results in an exothermic curve.

One endothermic curve due to the phase transition of AP (~244–250 °C) and two exothermic curves (250–350 °C) because of the thermal decomposition of AP were observed in the DSC thermogram of $CuZnCo_2O_4$ + AP (Fig. 10b). The peak temperature of exothermic curves appeared at ~270 °C (for LTD) and ~320 °C (HTD) for $CuZnCo_2O_4$ + AP, both of which were significantly lower than the decomposition peak temperature of pure AP. For $CuZnCo_2O_4$ + GO + AP (Fig. 11b), two endothermic curves: first because of the removal of water (<100 °C) and second because of the phase transition peak (~244–250 °C), and one exothermic curve (290–320 °C) was observed in the DSC curve with a peak temperature of 300 °C. For NTO, the overall weight losses in the presence of $CuZnCo_2O_4$ and $CuZnCo_2O_4$ + GO were found around ~60% (40% mass loss) to 20% (80% mass loss) while for AP, the overall weight losses in the presence of the above-mentioned catalysts were found around ~10% (90% mass loss), respectively.

The exothermic decomposition stages of AP and NTO were notably lowered after the addition of the four nanocatalysts ($NiCuZnCo_2O_4$, $NiCuZnCo_2O_4$ + GO, $CuZnCo_2O_4$, and

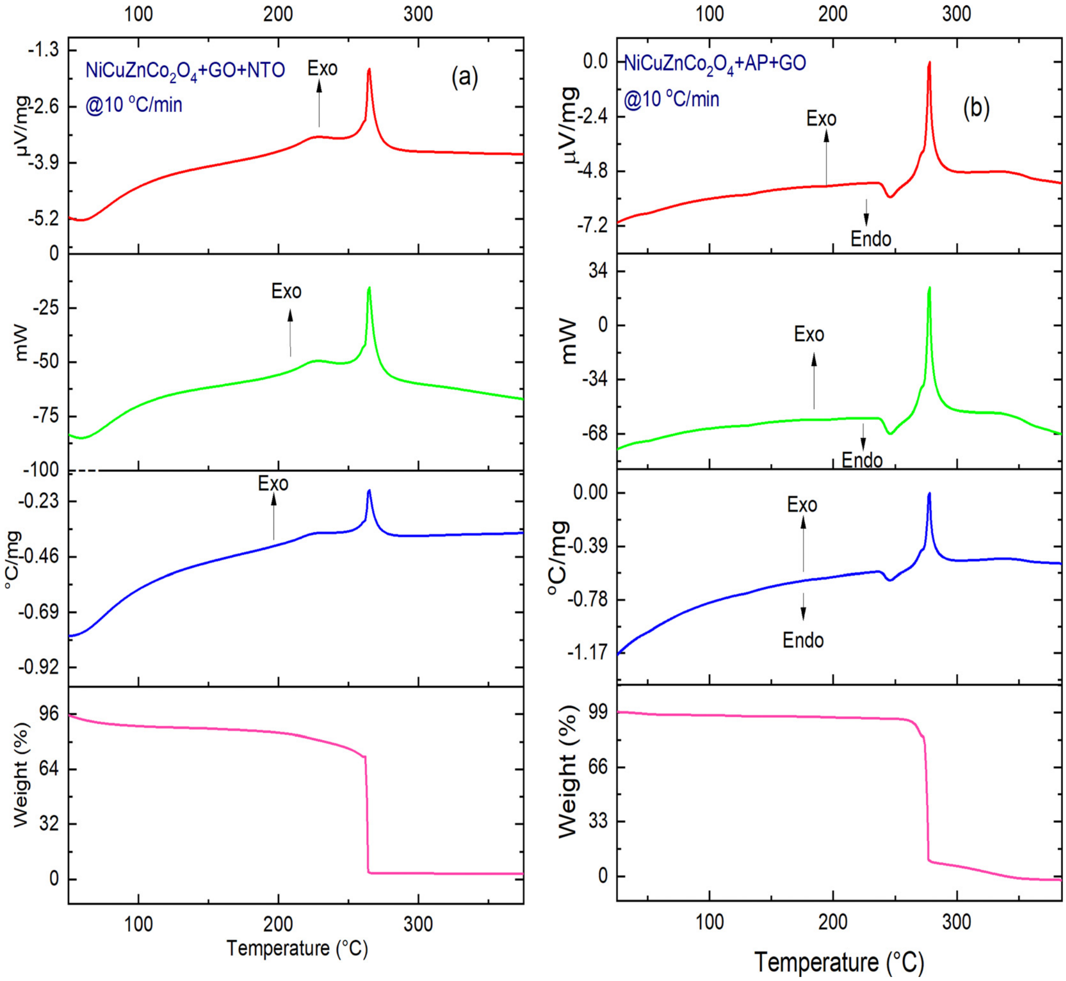

Fig. 9 TG-DTA-DSC thermographs of (a) $NiCuZnCo_2O_4$ + GO + NTO and (b) $NiCuZnCo_2O_4$ + GO + AP at a heating rate of 10 °C min^{-1}.

$NiCuZnCo_2O_4$ + GO) compared with those of pure AP and NTO. According to the DSC data, these nanocatalysts can effectively decrease the exothermic decomposition temperature of AP and NTO (Table 1). The order of peak decomposition temperature for NTO samples was found as follows: NTO > $NiCuZnCo_2O_4$ + GO + NTO > $NiCuZnCo_2O_4$ + NTO > $CuZnCo_2O_4$ + NTO > $CuZnCo_2O_4$ + GO + NTO. From the DSC results, $CuZnCo_2O_4$ + NTO was found to decompose at the lowest temperature. Moreover, the decomposition of $CuZnCo_2O_4$ + NTO occurs over a wide temperature range, making its use difficult in propulsion applications. Hence, comparatively, the composition of $CuZnCo_2O_4$ + GO + NTO was best suited as it decomposes in a single step at a 56 °C lower temperature than that of pure NTO. Moreover, the presence of Ni^{2+} in $CuZnCo_2O_4$ may have contributed to a stabilizing effect causing the thermal decomposition of NTO in the presence of $NiCuZnCo_2O_4$ to occur at a higher temperature than in the presence of $CuZnCo_2O_4$. The exothermic peak corresponding to the decomposition temperature of APs' samples followed the following order: AP > $CuZnCo_2O_4$ + AP > $NiCuZnCo_2O_4$ + AP = $CuZnCo_2O_4$ + GO + AP > $NiZnCo_2O_4$ + GO + AP.

Except for AP and AP + $CuZnCo_2O_4$, one exothermic curve was obtained for all three samples. This could be due to the merger of LTD and HTD. Moreover, the decomposition of $NiZnCo_2O_4$ + GO + AP was not completed up to 400 °C (lower mass loss). Hence, it could not provide the required propulsion. Hence, $NiZnCo_2O_4$ + GO + AP and $CuZnCo_2O_4$ + GO + AP were best suited for low-temperature, one-stage decomposition propulsion applications. Due to the Jahn–Teller effect of binary spinel full-filled cobaltite $CuZnCo_2O_4$, the redox and electron mechanism were effectively taken place in the presence of GO for thermolysis of NTO and AP. Thus, it can be said that the $CuZnCo_2O_4$ + GO catalyst was best-suitable for the thermolysis of both NTO and AP.

The comparative catalytic activity for the thermal decomposition of ammonium perchlorate (AP) and nitrotriazolone (NTO) of various transition metal oxides with those from this work is listed in Table 1.

Based on studies conducted in recent years,[43–45,47] two major mechanisms have been proposed for the thermal decomposition of ammonium perchlorate. First: electron transfer from the perchlorate ion to the ammonium ion and proton transfer from the ammonium ion to the perchlorate ion. Here,

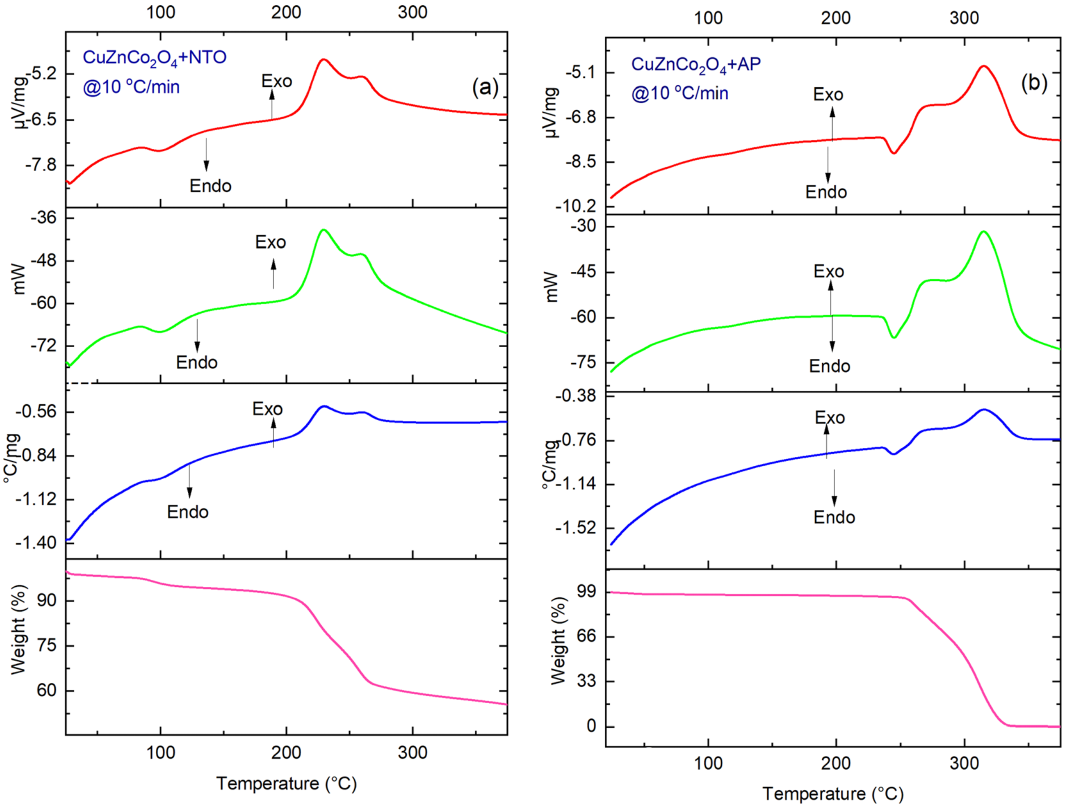

Fig. 10 TG-DTA-DSC thermographs of (a) $CuZnCo_2O_4$ + NTO and (b) $CuZnCo_2O_4$ + AP at a heating rate of 10 °C min^{-1}.

binary-ternary cobaltite nanomaterials with and without GO-positive holes on the catalyst surface accelerate the electron transfer from perchlorate ions over these effective active sites. Thus, these catalysts followed the electron transfer mechanism for AP decomposition and the C–NO_2 bond and ring cleavage for the thermolysis of NTO. Among the above-discussed catalysts, $NiCuZnCo_2O_4$ + GO plays a better catalytic role in APs' thermal decomposition and $CuZnCo_2O_4$ + GO plays a better catalytic role in NTO thermal decomposition. The reason behind their excellent catalytic performance was the synergistic catalytic effect of binary and ternary metal oxides that can easily accept the released electrons from oxidized ions or perchlorate ions, while cobaltites with GO provide additional electron acceptance active sites that improve the decomposition process of AP and NTO. Moreover, we propose that the existence of only lattice defects in the spinel cobaltite nanomaterials, such as $NiCuZnCo_2O_4$ and $CuZnCo_2O_4$, probably creates positive holes and electrons while $NiCuZnCo_2O_4$ + GO and $CuZnCo_2O_4$ + GO exist with additional p-type semiconducting GO molecules that create more holes that were responsible for enhancing the decomposition rate of AP and NTO.[37,38] $NiCuZnCo_2O_4$ + GO and $CuZnCo_2O_4$ + GO in comparison with $NiCuZnCo_2O_4$ and $CuZnCo_2O_4$ can produce more reduced species and positive holes on its surface and accelerate the AP and NTO thermal decomposition more than others.[43–45,47] Overall, the catalytic roles that spinel cobaltite nanomaterials, with and without GO additive, play in the AP and NTO decomposition are still more interesting for researchers.[41–47]

To study the catalytic and kinetic properties of spinel cobaltite nanomaterials $NiCuZnCo_2O_4$, $CuZnCo_2O_4$, $NiCuZnCo_2O_4$ + GO, and $CuZnCo_2O_4$ + GO for the thermal decomposition of AP and NTO, the high-temperature exothermic decomposition peak was considered from the DSC curves of AP and NTO. The kinetic parameters such as activation energy and Arrhenius constant can be calculated from the following relation (eqn (4)):[41] Slope of the plot of ln $\beta/T_p{}^2$ against $1/T_p$ was used to calculate the activation energy (E_k) by incorporating the value of the universal gas constant R.

$$\ln\frac{\beta}{T_P{}^2} = \ln\frac{RA}{E_K} - \frac{E_K}{R}\frac{1}{T_P} \qquad (4)$$

Here T_p is the peak temperature (K), β is the heating rate (°C min^{-1} or K min^{-1}), R is the gas constant (kJ K^{-1} mol^{-1}), E_a is the activation energy, and A is the preexponential factor. E_a values of pure AP and pure NTO are 167 ± 7 kJ mol^{-1} and 380 ± 20 kJ mol^{-1}, respectively. E_a values of AP in the presence of nanomaterials such as $NiCuZnCo_2O_4$, $NiCuZnCo_2O_4$ + GO, $CuZnCo_2O_4$, and $CuZnCo_2O_4$ + GO are 118 ± 5 kJ mol^{-1}, 95 ± 4 kJ mol^{-1}, 130 ± 6 kJ mol^{-1}, and 118 ± 5 kJ mol^{-1}, respectively. E_a values of NTO in the presence of nanomaterials such as $NiCuZnCo_2O_4$, $NiCuZnCo_2O_4$ + GO, $CuZnCo_2O_4$, and $CuZnCo_2O_4$ + GO are 298 ± 10 kJ mol^{-1}, 318 ± 7 kJ mol^{-1}, 236 ± 3 kJ mol^{-1}, and 229 ± 3 kJ mol^{-1}, respectively. This is a significant result because the decomposition of AP and NTO in the presence of these nanomaterials should be initiated faster than the decomposition of pure AP and NTO.

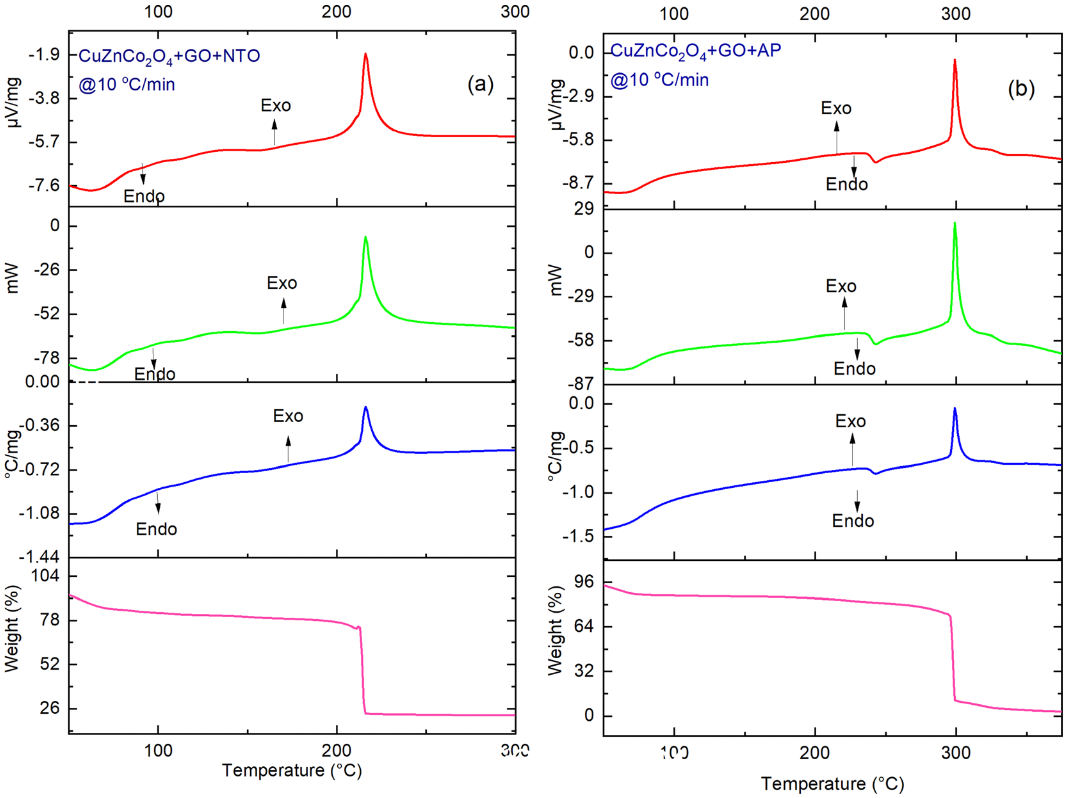

Fig. 11 TG-DTA-DSC thermographs of (a) CuZnCo$_2$O$_4$ + GO + NTO and (b) CuZnCo$_2$O$_4$ + GO + AP at a heating rate of 10 °C min^{-1}.

Table 1 Comparison of the catalytic activity for thermolysis of AP and NTO of various transition metal oxides

Samples	Catalyst (%)	HTD peak (°C)		Decrease of HTD peak (°C)	Single exothermic peak (°C)		Decrease of exothermic peak (°C)
		Pure AP	AP + sample		Pure NTO	NTO + sample	
CuCo$_2$O$_4$[46]	2	~471	~309	~162	—	—	—
Co$_3$O$_4$[43]	2	~444	~352	~92	—	—	—
CuFe$_2$O$_4$[48]	2	~445	~354	~91	—	—	—
T-Co and GO-T-Co-T[13]	20 mg	—	—	—	~274	~269 ~268	~5 ~6
NiCuZnCo$_2$O$_4$$^{\text{this work}}$	2	~440	~300	~140	~276	~250	~26
NiCuZnCo$_2$O$_4$ + GO$^{\text{this work}}$	2	~440	~276	~164	~276	~265	~11
CuZnCo$_2$O$_4$$^{\text{this work}}$	2	~440	~320	~120	~276	~225	~51
CuZnCo$_2$O$_4$ + GO$^{\text{this work}}$	2	~440	~300	~140	~276	~220	~56

Notes: HTD – high temperature decomposition; T – triaminoguanidine; E_a – activation energy

4. Conclusions

The polycrystalline spinel cobaltite NiCuZnCo$_2$O$_4$ and CuZnCo$_2$O$_4$ with a size of 9 nm to 28 nm and their mixtures with GO (NiCuZnCo$_2$O$_4$ + GO and CuZnCo$_2$O$_4$ + GO) were successfully synthesized. The direct bandgap of these nanocatalysts was found to be between 4 eV to 6 eV. Both NiCuZnCo$_2$O$_4$ and CuZnCo$_2$O$_4$ and their mixture with GO were able to decrease both the activation energy barrier as well peak decomposition temperatures of AP and NTO. Catalyst Mixtures such as CuZnCo$_2$O$_4$ + GO and NiCuZnCo$_2$O$_4$ + GO exhibit a better effect on the thermal decomposition of AP. Both catalysts were able to downshift the peak decomposition temperature of AP by >140 °C with a reduction in the activation energy (>40 kJ mol^{-1}) compared to pure AP. CuZnCo$_2$O$_4$ + GO + NTO showed a better thermal performance than pure NTO and its composition with NiCuZnCo$_2$O$_4$, NiCuZnCo$_2$O$_4$ + GO, and CuZnCo$_2$O$_4$. The peak decomposition temperature of CuZnCo$_2$O$_4$ + GO + NTO was decreased by 56 °C and the activation energy barrier was lowered by ~1.6–1.7 times than that of pure NTO. Thus, GO mixed with spinel cobaltite is a good carrier to accelerate electrons during the thermolysis of such propellant oxidizers that may be further applied for the preparation of various chemical propulsion systems in rocket science.

Data availability statement

All data generated or analyzed during this study are included in this published article.

Author contributions

PND has contributed to the conception and design of the work and finalization of the manuscript, RS has contributed to the acquisition, analysis, and interpretation of data, collection of XRD and Raman data, and writing the draft manuscript.

Conflicts of interest

The authors declare no competing financial and/or non-financial interests in relation to the work described.

Acknowledgements

RS thanks the Department of Science and Technology, Government of India, New Delhi, for financial assistance under Project file No. SR/NM/NT-1014/2016 (G)) funded by the Department of Science and Technology, New Delhi, India. Both authors appreciate the Department of Physics and Department of Chemistry, Sardar Patel University, Vallabh Vidyanagar, Gujarat, for providing laboratory and instrumental facilities. We thank UGC, New Delhi for the central thermal measurement facility sponsored under UGC-CAS (Phase-II) program grant vide sanction letter no. F. 540/5/CAS-II/2018(SAP-I) dated 25th July 2018. The authors are thankful to SICART, Vallabh Vidyanagar for the SEM facility.

References

1 M. T. Ahsan, M. Usman, Z. Ali, S. Javed, R. Ali, M. U. Farooq, M. A. Akram and A. Mahmood, *Front. Chem.*, 2020, **8**, 487.

2 T. M. Hammad, S. Kuhn, A. A. Amsha, N. K. Hejazy and R. Hempelmann, *J. Supercond. Novel Magn.*, 2020, **33**, 3065–3075.

3 A. F. Abdulaziz, K. I. Khaleel and N. A. Bakr, *Tikrit J. Pure Sci.*, 2011, **16**, 216–222.

4 S. S. Shetgaonkar, A. V. Salkar and P. P. Morajkar, *Chem. – Asian J.*, 2021, **16**, 2871–2895.

5 E. B. F. Galante, N. Mai, M. K. Ladyman, P. P. Gill, T. J. Temple and F. Coulon, *J. Energ. Mater.*, 2021, **39**, 85–99.

6 A. Benhammada, D. Trache, S. Chelouche and A. Mezroua, *Z. Anorg. Allg. Chem.*, 2021, **647**, 312–325.

7 A. Benhammada, D. Trache, M. Kesraoui, A. F. Tarchoun, S. Chelouche and A. Mezroua, *Thermochim. Acta*, 2020, **686**, 178570.

8 J. Bhagwan, G. Nagaraju, B. Ramulu, S. C. Sekhar and J. S. Yu, *Electrochim. Acta*, 2019, **299**, 509–517.

9 S. V. Bhatt, M. Deshpande, V. Sathe, R. Rao and S. Chaki, *J. Raman Spectrosc.*, 2014, **45**, 971–979.

10 P. Chand, S. Vaish and P. Kumar, *Phys. B*, 2017, **524**, 53–63.

11 S. Hanafi, D. Trache, W. He, W.-X. Xie, A. Mezroua and Q.-L. Yan, *Thermochim. Acta*, 2020, **692**, 178747.

12 H. Kechit, S. Belkhiri, A. K. Bhakta, D. Trache, Z. Mekhalif and A. F. Tarchoun, *Z. Anorg. Allg. Chem.*, 2021, **647**, 1607–1619.

13 S. Hanafi, D. Trache, W. He, W.-X. Xie, A. Mezroua and Q.-L. Yan, *J. Phys. Chem. C*, 2020, **124**, 5182–5195.

14 S. Bekhouche, D. Trache, A. Abdelaziz, A. F. Tarchoun, S. Chelouche, A. Boudjellal and A. Mezroua, *Chem. Eng. J.*, 2023, **453**, 139845.

15 Y. Wang, X. Song and F. Li, *Nanomaterials*, 2019, **9**, 1605.

16 F. Chalghoum, D. Trache, M. Benziane and A. Benhammada, *FirePhysChem*, 2022, **2**, 36–49.

17 F. Chalghoum, D. Trache, M. Benziane and S. Chelouche, *J. Therm. Anal. Calorim.*, 2022, **147**, 11507–11534.

18 S. Hanafi, D. Trache, R. Meziani, H. Boukeciat, A. F. Tarchoun, A. Abdelaziz and A. Mezroua, *FirePhysChem*, 2022, **2**(4), 315–322.

19 T. Chen, Y. Hu, C. Zhang and Z. Gao, *Def. Technol.*, 2021, **17**, 1471–1485.

20 K. Lysien, A. Stolarczyk and T. Jarosz, *Materials*, 2021, **14**, 6657.

21 T. Dippong, E.-A. Levei, C. L. Lengauer, A. Daniel, D. Toloman and O. Cadar, *Mater. Charact.*, 2020, **163**, 110268.

22 A. A. Rodríguez-Rodríguez, M. B. Moreno-Trejo, M. J. Meléndez-Zaragoza, V. Collins-Martínez, A. López-Ortiz, E. Martínez-Guerra and M. Sánchez-Domínguez, *Int. J. Hydrogen Energy*, 2019, **44**, 12421–12429.

23 W.-C. Oh and F.-J. Zhang, *Asian J. Chem.*, 2011, **23**, 875–879.

24 S. Farhadi, J. Safabakhsh and P. Zaringhadam, *J. Nanostruct. Chem.*, 2013, **3**, 69.

25 Q. Li, Y. Wang and C. Chang, *J. Alloys Compd.*, 2010, **505**, 523–526.

26 T. Mukundan, G. Purandare, J. Nair, S. Pansare, R. Sinha and H. Singh, *Def. Sci. J.*, 2002, **52**, 127.

27 S. S. Selima, M. Khairy and M. A. Mousa, *Ceram. Int.*, 2019, **45**, 6535–6540.

28 S. Thoka, C.-J. Chen, A. Jena, F.-M. Wang, X.-C. Wang, H. Chang, S.-F. Hu and R.-S. Liu, *ACS Appl. Mater. Interfaces*, 2020, **12**, 17353–17363.

29 H. X. Zhao, B. M. He, J. Li, H. M. Jia and L. W. Mi, *Adv. Mater. Res.*, 2012, **512–515**, 2467–2470.

30 X.-L. Zhou, P.-J. He, W. Peng, F. Lü, L.-M. Shao and H. Zhang, *J. Anal. Appl. Pyrolysis*, 2022, **161**, 105421.

31 J. P. Agrawal, *High Energy Materials: Propellants, Explosives and Pyrotechnics*, John Wiley & Sons, 2010.

32 V. V. Boldyrev, *Thermochim. Acta*, 2006, **443**, 1–36.

33 A. R. Patel, G. Sereda and S. Banerjee, *Curr. Pharm. Biotechnol.*, 2021, **22**, 773–792.

34 X. Xiao, G. Zhang, Z. Wang, Y. Zhu, Z. Yan and Y. Wang, *J. Alloys Compd.*, 2022, **908**, 164624.

35 H. Feng, X. Liu, Y. Li, X. Ma, Q. Yan and F. Zhao, *Powder Technol.*, 2022, **397**, 117035.

36 F. Yang, J. Pei and H. Zhao, *Langmuir*, 2022, **38**, 3844–3851.

37 H. Akbi, S. Rafai, A. Mekki, S. Touidjine, M. Fertassi and D. E. Kadri, *J. Organomet. Chem.*, 2022, **957**, 122159.

38 Y. Chao, W. Peng, W. Wang, X. Zhang and Y. Cao, *Appl. Nanosci.*, 2022, **12**, 3177–3184.

39 B.-R. Jheng, P.-T. Chiu, S.-H. Yang and Y.-L. Tong, *Sci. Rep.*, 2022, **12**, 2921.

40 D. Mladenović, E. Daş, D. M. F. Santos, A. B. Yurtcan, Š. Miljanić and B. Šljukić, *J. Alloys Compd.*, 2022, **905**, 164156.

41 S. Gedi, R. Manne, G. Manjula, L. V. Reddy, C. P. Reddy, N. Marraiki, W. K. Kim, K. Mallikarjuna and M. S. Pratap Reddy, *J. Phys. Chem. Solids*, 2022, **163**, 110587.

42 N. M. Juibari and S. Tarighi, *J. Therm. Anal. Calorim.*, 2018, **133**, 1317–1326.

43 E. Alizadeh-Gheshlaghi, B. Shaabani, A. Khodayari, Y. Azizian-Kalandaragh and R. Rahimi, *Powder Technol.*, 2012, **217**, 330–339.

44 M. R. S. A. Janjua, *Open Chem.*, 2019, **17**, 865–873.

45 B. C. Beard and J. Sharma, *J. Energ. Mater.*, 1993, **11**, 325–343.

46 X. Xiao, Z. Zhang, L. Cai, Y. Li, Z. Yan and Y. Wang, *J. Alloys Compd.*, 2019, **797**, 548–557.

47 J. Gaete, J. L. Arroyo, Á. Norambuena, G. Abarca and C. Morales-Verdejo, *Inorg. Chem.*, 2022, **61**, 1447–1455.

48 T. Liu, L. Wang, P. Yang and B. Hu, *Mater. Lett.*, 2008, **62**(24), 4056–4058.